

35 Introduction

36 The Tibetan Plateau (TP), which resembles a "third pole" and a "world water
37 tower", plays an important and special role in the global climate and energy–water
38 cycle (Xu et al., 2008; Wu et al., 2015). The TP covers a quarter of China.
39 Additionally, the average altitude of the TP is 4000 meters, reaching 1/3 of the
40 tropopause height, so it is called the "World Roof". Cumulus convection over the TP
41 transfers heat, moisture and momentum into the free troposphere, which can impact
42 the atmospheric circulation regionally and globally (Li and Zhang, 2016; Xu et al.,
43 2014) and reveals the important "window effect" for the transfer and exchange of
44 global energy and water vapor over the TP. The special heat source dynamic effect
45 constitutes the "window effect" and "thermally driven" mechanism over the TP.

46 The results of the TIPEX II, which was carried out in 1998, showed that the strong
47 convective plumes within PBL observed by sodar and a frequently occurred deep
48 mixed layer (>2 km) can lead to ubiquitous "popcorn - like" cumulus clouds in
49 Dangxiong, and Xu et al. (2002) proposed a comprehensive physical pattern of
50 land-air dynamic and thermal structure on the Qinghai-Xizang Plateau (Xu et al.,
51 2002; Zhou, 2000). The previous studies have done many valuable researches on the
52 triggering mechanism of moist convection over moist and dry surfaces based on
53 atmospheric observations and simulations (Ek and Mahrt, 1994; Findell and Eltahir,
54 2003; Gentine et al., 2013). For dry surface, the weak stratification and strong
55 sensible heat flux result in the rapid growth of PBLH so that the relative humidity at
56 the top of the boundary layer RH_{top} increases rapidly, which favors the formation of
57 clouds. For moist surface, strong stratification and evaporation (small bowen ratio)
58 result in slow growth of PBLH, also increase the mixed layer specific humidity and
59 RH_{top} , which favor the formation and development of clouds. Taylor et al. (2012)
60 found that the afternoon rain falls preferentially over soils that are relatively dry
61 compared to the surrounding area, especially for semi-arid regions. Guillod et al.
62 (2015) reconciled spatial and temporal soil moisture effects on the afternoon rainfall.
63 They showed that afternoon precipitation events tend to occur during wet and
64 heterogeneous soil moisture conditions, while being located over comparatively drier
65 patches. Tuttle et al. (2016) showed the empirical evidence of contrasting soil
66 moisture–precipitation feedbacks across the United States, and they found that soil
67 moisture anomalies significantly influence rainfall probabilities over 38% of the area
68 with a median factor of 13%. According to the model results over dry and wet soils in
69 Illinois, Findell et al. (2003) summarized the predictive capability of rain and shallow
70 clouds gained from use of the convective triggering potential (CTP) and a low-level
71 humidity index, HI_{low} as measures of the early morning atmospheric setting. Our
72 previous studies pointed out that the developments of these cumulus clouds are related
73 to the special large scale dynamic structure and turbulence within PBL over the TP
74 (Xu et al., 2014; Wang et al., 2020). All the above results indicate the topography of
75 the TP plays a major role in increasing the occurrence frequency of the strong

76 convective clouds (Luo et al., 2011). This conclusion is consistent with the viewpoint
77 of Flohn (1967) who emphasized the chimney effect of the huge cumulonimbus
78 clouds on heat transfer in the upper troposphere.

79 The TP is one of the regions in China where high frequency of cumulus clouds
80 occurs, and the development of cumulus system is related to both the turbulence and
81 special dynamical structure in PBL over the TP. The vertical motion over the TP is
82 associated with the anomalous convective activities. However, as Li and Zhang (2016)
83 mentioned, the details of PBL process are not very clear, and also the diurnal
84 variations and formation mechanism of low clouds over the TP and low elevation
85 regions are still not very clear. The different variation characteristics of these low
86 clouds at different elevations also need to be discussed and analyzed. We further need
87 to discuss whether there exist “high efficiency” triggering mechanisms for convection
88 over the TP, and whether there is an association among low air density, strong
89 turbulence and ubiquitous “popcorn-like” cumulus clouds. Is there also strong
90 turbulence at higher elevation region with lower air density in the globe? Because
91 both the TP and Rocky Mountains are high elevation regions with huge area in
92 mid-latitude, in this study we mainly focus on these two regions to analyze the above
93 scientific questions.

94 **2 Observational and reanalysis data**

95 We use in situ measurements of temperature (T) and relative humidity (RH) at 2 m
96 height, surface pressure data every hour, and low cloud cover (LCC) every three
97 hours from 2402 automatic weather stations from June to August of 2010-2019 in
98 China. LCC here refers to the fraction of the sky covered by low clouds as estimated
99 by human observers, including five cloud types: nimbostratus (Ns), stratocumulus
100 (Sc), stratus (St), cumulus (Cu), and deep convection (DC). These surface observation
101 datasets are provided by China National Meteorological Information Center.

102 In addition, we use the hourly $0.25^\circ \times 0.25^\circ$ ERA5 reanalysis surface-layer data
103 in summer (June 1 to August 31) from 2010 to 2019 (Hersbach et al., 2020).

104 We use more than 4 years (from June 15 2006 to August 31 2010) of the satellite
105 (CloudSat radar and Calipso lidar)-merged cloud classification product
106 2B-CLDCLASS-lidar to calculate the mean LCC with $1^\circ \times 1^\circ$ resolution at about 2:00
107 pm and 2:00 am LT in summer. The introduction of this product and details of the
108 LCC calculation methods are summarized in Sassen and Wang (2008) and Wang et al
109 (2020).

110 We use a Gaofen 4 (GF 4) visible satellite image with spatial resolution of 50 m
111 on August 4 in 2020 to show the organized structures (cellular convection) in
112 southeastern TP. GF 4 is a geostationary earth observation satellite in the Gaofen
113 series of Chinese civilian remote sensing satellites. We also use the 1 year (from June
114 1 to August 31 in 2016) geostationary satellite himawari-8 retrieval product (cloud top
115 height) over land in East Asia.

116 In this study, we also use monthly mean temperature (T) and relative humidity
117 (RH) at 2 m height, surface pressure, planetary boundary layer height (PBLH) every

118 hour from ERA5 reanalysis data from 2010 to 2019. The lifting condensation level
 119 (LCL) is calculated by method proposed by (Romps, 2017).

120 Using sensible heat flux H , Northward turbulent surface stress τ_y and Eastward
 121 turbulent surface stress τ_x from ERA5 reanalysis data, then we calculate the
 122 buoyancy term (BT) ($g/\theta_v \overline{w'\theta'_v}$) and shear term (ST) ($-\partial\bar{u}/\partial z \overline{u'w'}$) in the TKE
 123 equation for each grid. Both of these two terms can be used to analyze the effect of
 124 boundary layer turbulence in surface layer on convection. The details of the method
 125 for computing BT and ST are as follows:

126 The shear term (ST) ($-\partial\bar{u}/\partial z \overline{u'w'} - \partial\bar{v}/\partial z \overline{v'w'}$) and buoyancy term (BT) ($g/\theta_v \overline{w'\theta'_v}$)
 127 in the TKE equation maintain the turbulent motions. In order to simplify calculations,
 128 the x-axis is directed along the average wind. Assuming horizontal homogeneity and
 129 no mean divergence, the TKE equation is written as

$$130 \quad \frac{\partial \bar{e}}{\partial t} = \frac{g}{\theta_v} \overline{w'\theta'_v} - \overline{u'w'} \frac{\partial \bar{u}}{\partial z} - \frac{\partial(\overline{w'e})}{\partial z} - \frac{1}{\rho} \frac{\partial(\overline{w'p'})}{\partial z} - \varepsilon. \quad (1)$$

131 The left side of eq. (1) is the local time variation $\partial\bar{e}/\partial t$, and the terms on the
 132 right-hand side of eq. (1) describe the buoyancy and shear energy production or
 133 consumption, turbulent transport of \bar{e} , pressure correlation and viscous dissipation
 134 (Stull, 1988).

135 Here we use eq. (2) to calculate virtual potential temperature θ_v , and $\overline{w'\theta'_v}$ is
 136 derived from eq. (3). Finally, we derive BT.

$$137 \quad \theta_v = T(1 + 0.608q) \left(\frac{p_0}{p} \right)^{\frac{R}{c_p}}, \quad (2)$$

$$138 \quad H = \rho c_p \overline{w'\theta'_v}, \quad (3)$$

139 Where $g = 9.8 \text{ m s}^{-2}$ is the gravitational constant, and $H \text{ (W m}^{-2}\text{)}$ is the sensible heat
 140 flux, $\rho \text{ (kg m}^{-3}\text{)}$ is the air density, R is the specific gas constant for dry air, $c_p \text{ (=1004 J}$
 141 $\text{kg}^{-1} \text{ K}^{-1}\text{)}$ is the specific heat of air at constant pressure, T is the air temperature at 2 m
 142 height, q is the specific humidity at 2 m height, p_0 and p are standard atmospheric
 143 pressure and surface pressure, respectively.

144 The $\partial\bar{u}/\partial z$ in the surface layer is estimated as

$$145 \quad \frac{\partial \bar{u}}{\partial z} = \phi_m(\zeta) \frac{u_*}{kz}, \quad (4)$$

146 and the non-dimensional wind profiles ϕ_m (Dyer, 1974) is :

$$147 \quad \phi_m = 1 + 5\zeta, (\zeta > 0) \quad (5)$$

148
$$\phi_m = (1 - 16\zeta)^{-1/4}, (\zeta < 0) \quad (6)$$

149
$$\zeta = \frac{z}{L}, L = \frac{-u_*^3}{\kappa \frac{g}{\theta_v} w' \theta'_v}, \quad (7)$$

150
$$\tau = \sqrt{\tau_x^2 + \tau_y^2}, \quad (8)$$

151
$$\tau = \rho u_*^2, \quad (9)$$

152
$$\tau = -\rho \overline{u'w'}. \quad (10)$$

153 Where the von Karman constant $\kappa=0.4$, and $z = 10$ m. \bar{u} is the horizontal wind
 154 speed at level z and u_* is the frictional velocity. The stability parameter z/L is defined
 155 in eq. (7). τ_x and τ_y are the Eastward and Northward turbulent surface stress,
 156 respectively. τ is turbulent fluxes of momentum, which can be calculated by using eq.
 157 (8). Then we use eq. (9) to derive u_* . We also use eq. (10) to derive $-\overline{u'w'}$. Finally,
 158 we derive ST.

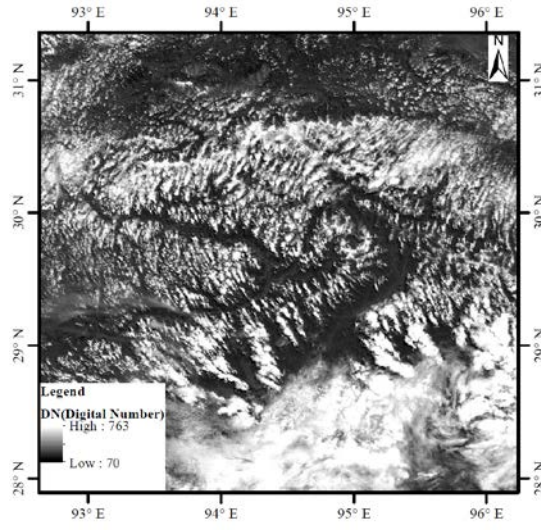
159

160 3 Results

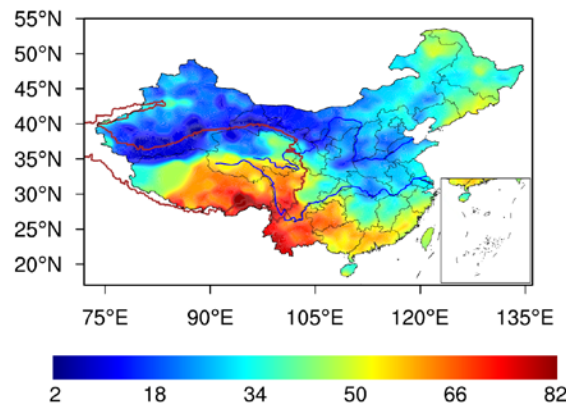
161 Figure 2 shows the spatial distribution of over-land low cloud cover (LCC) in
 162 China from June to August of 1951-2019. The high value areas of LCC are mainly
 163 located in the eastern TP and the area of the upper Yangtze River Valley. Using four
 164 years of CloudSat-Calipso satellite data, Li and Zhang (2016) also confirmed that the
 165 climatological occurrence of cumulus over the TP is significantly greater than that in
 166 mid-eastern China on the same latitude. The elevated land surface with strong
 167 radiative heating makes the massive TP a favorable region for initiating convective
 168 cells with a high frequency of cumulonimbus and mesoscale convective systems
 169 (Sugimoto and Ueno, 2012). As a strong heat source, the TP has frequent convective
 170 activities in summer. During the TIPEX II in 1998, the long and narrow thermal
 171 plume corresponding with vigorous cellular convection on micro-scale was observed
 172 by sodar in Dangxiong. As shown in Figure 1, the convective plume and “raised”
 173 cloud on a horizontal scale from hundreds of meters to several kilometres over the
 174 southeastern TP (above latitude 30N) are probably related to the organized eddies on
 175 the meso-scale and micro-scale over the TP.

176 As shown in Figure 3, in general, LCC increases with the increasing elevation.
 177 The median of LCC_H are significantly greater than those of LCC_L and LCC_M
 178 throughout the day. The diurnal variations of LCC_L and LCC_M are generally
 179 distributed in unimodal pattern with the maximum appearing at 2:00 pm BT (median
 180 $LCC_L = 37\%$, $LCC_M = 38\%$) and low values ($\sim 20\%$) are maintained during the night.
 181 The diurnal variation of LCC_H presents a bimodal curve with the maximum appearing

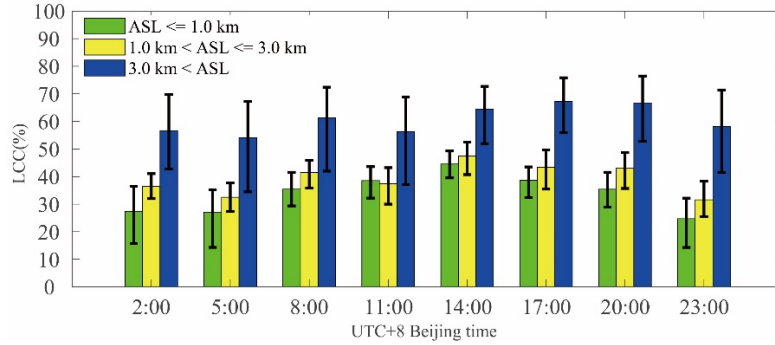
182 at 5:00 pm BT (median $LCC_H = 69\%$) and the secondary local maximum appearing at
 183 8:00 am BT (median $LCC_H = 61\%$). Compared to the low elevation, the interquartile
 184 ranges (IQRs) of LCC_H are less than those of LCC_L and LCC_M , which imply the
 185 LCC_H maintains high values during the day. To further confirm and compare the
 186 above results from in situ measurements, using ERA5 LCC data, we also add Figure
 187 S1 to show the diurnal cycle of LCC in summer in East Asia and North America in
 188 supplementary material.



189
 190 Figure 1. The digital number of geostationary earth observation satellite Gaofen 4
 191 (GF4) at 12:00 pm Beijing time (about 10:20 am local time) on August 4 in 2020 in
 192 southeastern TP.

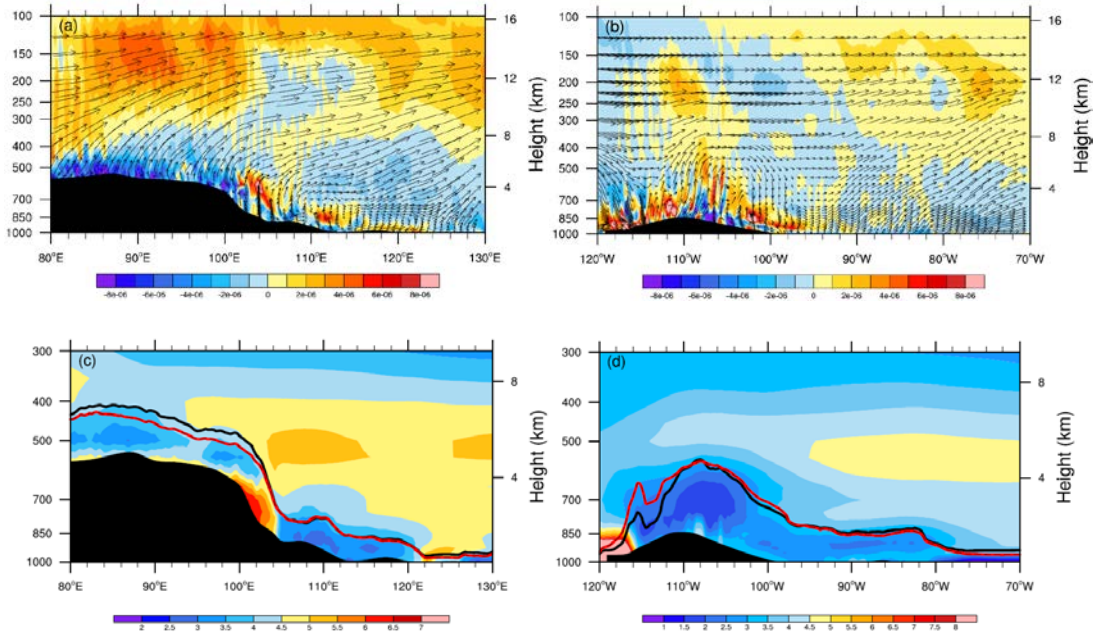


193
 194 Figure 2. The summer mean LCC derived from surface observations in summer from
 195 1951 to 2019 in China. The thick
 196 red contour denotes the 2.5 km topography height referred to as the TP. The blue lines
 197 located in northern and southern part of China denote the Yellow and Yangtze River,
 198 respectively.



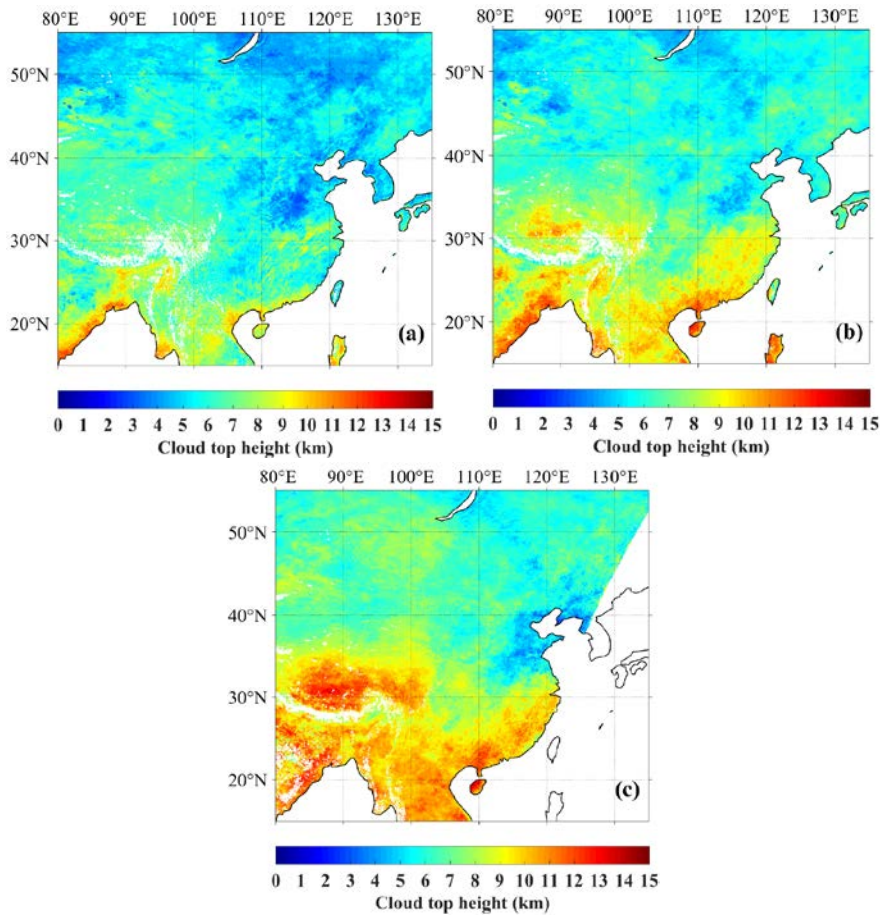
199
200
201
202
203
204
205
206

Figure 3. The diurnal cycle of LCC in summer from 2010 to 2019 at different altitudes above sea level (ASL): $ASL \leq 1.0$ km (LCC_L), $1.0 \text{ km} < ASL \leq 3.0$ km (LCC_M), and $3.0 \text{ km} < ASL$ (LCC_H). It should be noted that all the sites are ranged from 27N to 40N in China, and each sample is derived from monthly mean LCC at a particular time in summer for each site. The bar and error bar represent the median values and interquartile ranges (IQRs) of LCC, respectively.



207
208
209
210
211
212
213
214
215

Figure 4. Vertical distribution of divergence (s^{-1}) (shaded) at the latitude across sections from 30N to 35N in (a) East Asia, (b) North America. The summer mean vectors of U- and W- wind components at local time 2:00 pm from 2010 to 2019 along 30N–35N with the zonal circulations. The black shaded area represents topography. The red and black lines in Figure (c) and (d) denote the LCL and PBLH, respectively. The shaded colors except black in Figure (c) and (d) represent the vertical gradients of virtual potential temperature $d\theta_v/dz$.



216

217

218 Figure 5. The median cloud top height derived from himawari-8 retrieval product at
 219 three Beijing times: (a) 2:30 pm±0.5h (b) 4:30 pm±0.5h (c) 6:30 pm±0.5h from June
 220 to August in 2016 over land in East Asia. Missing data are shaded in white color.

221

222 On the other hand, we note that, compared to eastern China, there is no obvious
 223 decrease trend for the LCC over the TP from late afternoon to evening as shown in
 224 Figure 3. Based on the spatial distribution of topography in the Northern Hemisphere
 225 as shown in Figure 7 (a), it is clear that both the TP (27-40N, 70-105E) and Rocky
 226 Mountains (27-40N, 103-120W) in North America are two large area with high
 227 elevations in mid-latitude region in the Northern Hemisphere, so here we select these
 228 two typical large topography regions to analyze the triggering effects of large
 229 topography and related dynamical structure within the boundary layer on convective
 230 clouds. The Figure 4 (a) shows there are obvious large scale ascending motions from
 231 near surface layer to upper troposphere over the TP, which correspond with the
 232 convergence at 500 hPa and the divergence at 200 hPa. Figure 4 (c) shows there are
 233 deep weak inversion layer (about 2 km with $d\theta_v/dz < 3 \text{ K km}^{-1}$) and positive
 234 PBLH-LCL over the TP. These results are consistent with the conclusions proposed
 235 by Xu et al. (2014) and Wang et al. (2020). In contrast, Figure 4 (b) shows there are
 236 only weak large scale ascending motions from near surface layer to middle
 237 troposphere over the Rocky Mountains, while the large-scale subsidence on both sides
 238 of the Rocky Mountains leads to strong inversion above PBL and lower RH in near
 239 surface layer. The former restricts the growth of PBLH during the day, and the latter

240 leads to the increased LCL. Thus negative PBLH-LCL is identified on both sides of
241 the Rocky Mountains, especially for the western Rocky Mountain with strong
242 large-scale subsidence, as shown in Figure 4 (d). With its thermal structure, the TP
243 leads to dynamic processes of vapor transport, similar to the conditional instability of
244 the second kind (CISK) mechanism of tropical cyclones.

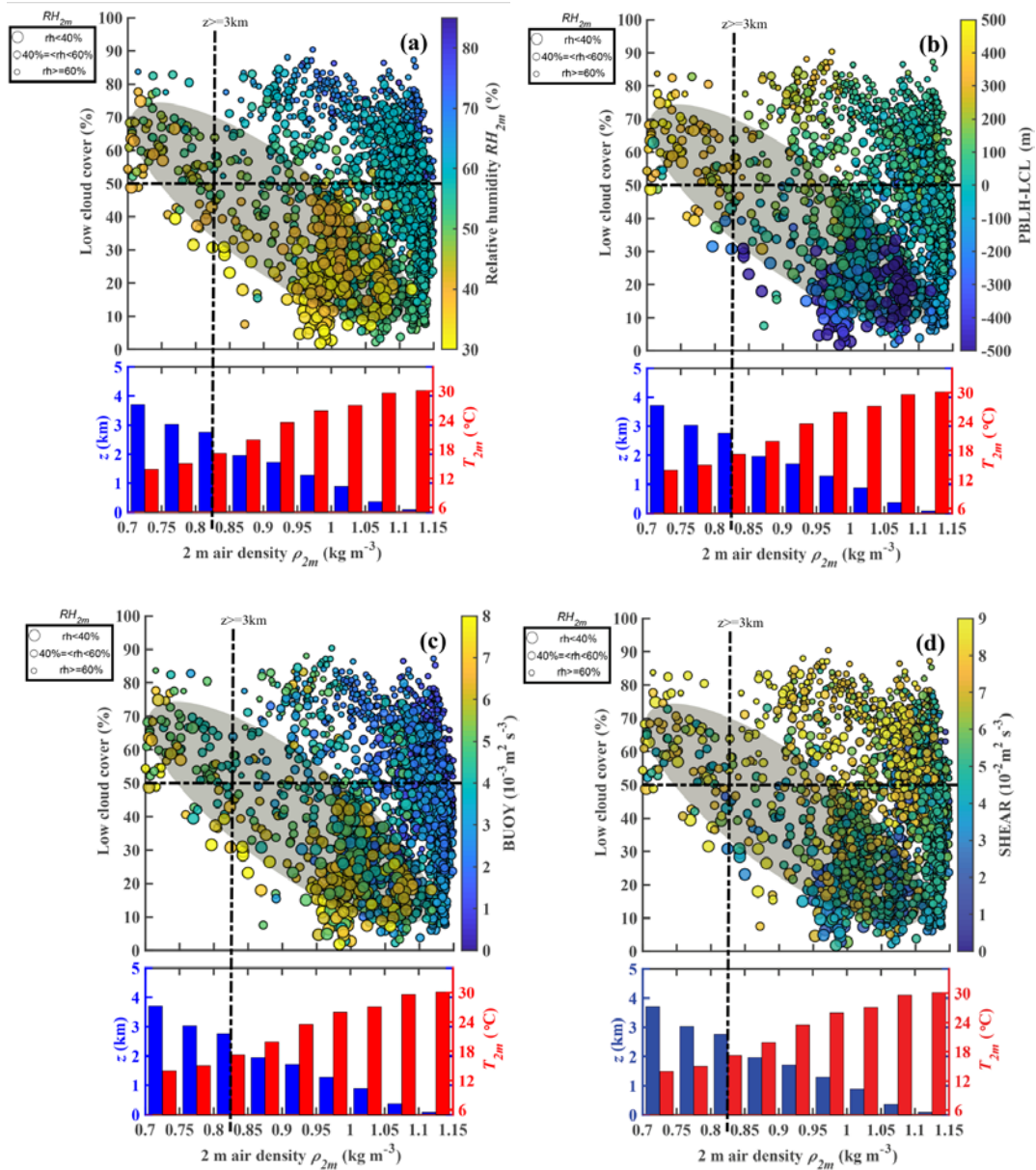
245 Figure 5 shows the spatial distribution of day time variations of cloud top height
246 in summer. Compared to eastern China at the same latitude, the cloud top height has a
247 significant increase from 2:30 pm (~7 km) to 6:30 pm (~14 km) over the TP. The
248 cloud top height approaches the tropopause (~14 km) in the evening over the TP,
249 which implies the frequent deep convective clouds at this time. This result is
250 consistent with the observation of millimeter-wave radar in Naqu (Yi, 2016).

251 By comprehensively analyzing the second Tibet Plateau Experiment (TIPEX II)
252 sodar data, Xu et al. (2002) and Zhou et al. (2000) found that, with narrow upward
253 motion and time scale from 1.2 h to 1.5 h, the maximum upward motion of the
254 thermal turbulence was identified at the height of about 120 m above the surface, its
255 vertical speed up to 1 m s^{-1} . They also found symmetrical and wide downward motion
256 area on either side of the narrow upward motion zone. The question arises as to
257 whether there is a relationship between the formation and evolution of frequent
258 "pop-corn-like" convective clouds and micro-scale thermal turbulence in the
259 atmospheric convective boundary layer over the TP. Xu et al., (2012) speculate these
260 low clouds are probably initiated by strong thermal turbulence under low air density
261 condition. Compared to the low elevation in eastern China, the increased thermal
262 turbulence associated with low air density over the TP leads to the different
263 turbulence characteristics of convective boundary layer (CBL). The CBL is mainly
264 driven by buoyancy heat flux, and thermal turbulence with organized thermal plume
265 is not totally random (Young, 1988a; Young, 1988b). The BT and ST over the TP are
266 significantly greater than those at the low elevation, which play key roles in the
267 convective activities in lower troposphere.

268 By using the statistical results from sodar data in the second Tibetan Plateau
269 Experiment for atmospheric sciences (TIPEX II), Zhou et al. (2000) calculated the BT
270 and ST at the height of 50 m under strong convection condition in Dangxiong (located
271 at central TP). The results indicate that the BT is comparable to ST. Both the
272 thermodynamic and dynamic processes have important influences on the convective
273 activities. Both the BT and ST in the surface layer in Dangxiong are almost an order
274 of magnitude greater than those at low elevation given by Brummer (1985) in North
275 Sea and Weckwerth et al. (1997) in Florida. Direct measurements from the Third
276 Tibetan Plateau Experiments (TIPEX III) also confirmed that surface buoyancy flux
277 over the TP is significantly larger than that in eastern China (Zhou, 2000; Wang et al.,
278 2016). Both the sodar data in TIPEX II and boundary layer tower data in TIPEX III
279 showed contributions of BT and ST to the turbulent kinetic energy in the lower
280 troposphere are larger over the TP than over the southeastern margin of the TP and the
281 low-altitude Chengdu Plain (Zhou, 2000; Wang et al., 2015). What is the relationship
282 between high frequent low cloud and the above physical quantities (e.g. turbulence
283 structure, temperature and humidity) under low air density condition over the TP? The

284 physical mechanism should be discussed and analyzed. In addition, at low elevation in
285 eastern China, the question arises as to whether or not the variations of PBLH and
286 LCL favor the formation and development of low clouds.

287 As shown in Figure 6 (a), compared to the low elevation, for low RH_{2m} condition
288 ($RH_{2m} < 40\%$), there is larger LCC ($LCC > 50\%$) over the TP ($ASL > 3$ km). In
289 contrast, larger LCC mostly corresponds to higher RH_{2m} condition at low elevation,
290 which is consisted with our common sense. The above interesting phenomenon can be
291 explained by the differences of PBLH-LCL between TP and low elevation on summer
292 afternoons, which are mainly attributed to two mechanisms. With a similar sensible
293 heat flux, the lower air density over the TP leads to greater surface buoyancy flux (or
294 BT) as shown in Figure 6 (c), which is conducive to the increase of PBLH over the
295 TP. Figure 6 (d) shows great ST over the TP, which is mainly attributed to large wind
296 speed. Although here we only show the ST in surface layer, strong wind shear in
297 boundary layer probably also plays a role in increasing PBLH over the TP. On the
298 other hand, with a similar RH, Wang et al. (2020) have indicated that, compared to the
299 low elevation in eastern China, the lower temperature over the TP leads to a lower
300 LCL. Together these mechanisms lead to a greater (PBLH-LCL) difference over the
301 TP on summer afternoons, which increase the probability of air parcels reaching the
302 LCL and forming clouds as shown in Figure 6 (b). For the TP, in most cases, the
303 positive value of PBLH-LCL, great BT and ST correspond larger LCC ($LCC > 50\%$)
304 for low $RH_{2m} < 60\%$, which implies the local more LCC is relevant to the diurnal
305 variation of the PBL process. In contrast, for the eastern China, in most cases, the
306 larger LCC ($LCC > 50\%$) generally correspond the high $RH_{2m} > 60\%$, and the LCC is
307 not significantly correlated with PBLH-LCL, BT and ST, which implies the other
308 factors besides the PBL process (e.g. large scale ascending motion) play a more
309 important in LCC.



310

311

312 Figure 6. The relationships among monthly means of low cloud cover LCC, ρ_{2m} and
 313 (a) RH_{2m} , (b) PBLH-LCL, (c) BT and (d) ST at 2:00 pm (BT) from 2010 to 2019 in
 314 summer in China. The samples are divided into three groups: $RH_{2m} \geq 60\%$ (small
 315 size dots), $60\% > RH_{2m} \geq 40\%$ (median size dots) and $RH_{2m} < 40\%$ (large size dots).
 316 The LCC, T_{2m} and RH_{2m} are observed by in situ measurements, and PBLH, LCL, BT
 317 and ST are derived from ERA5 reanalysis data. Here we use the nearest neighbor
 318 gridding method to derive the PBLH, LCL, BT and ST at each site. The blue and red
 319 histograms show an approximate relationship between ρ_{2m} and surface elevation
 320 above sea level z , air temperature at 2 m (T_{2m}) at the bottom of Figure 2a, respectively.
 321 The dots with lower RH_{2m} ($RH_{2m} < 40\%$) are mostly distributed within grey shaded
 322 elliptic region as shown in Figure 6 (a)-(d).

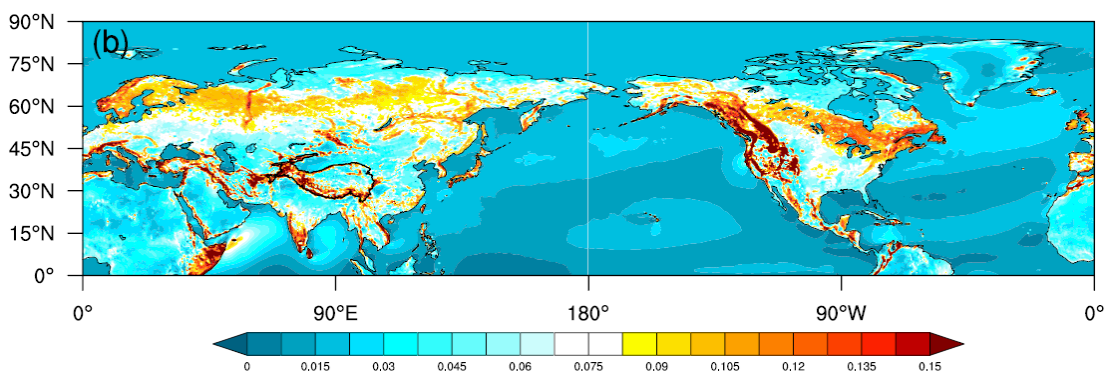
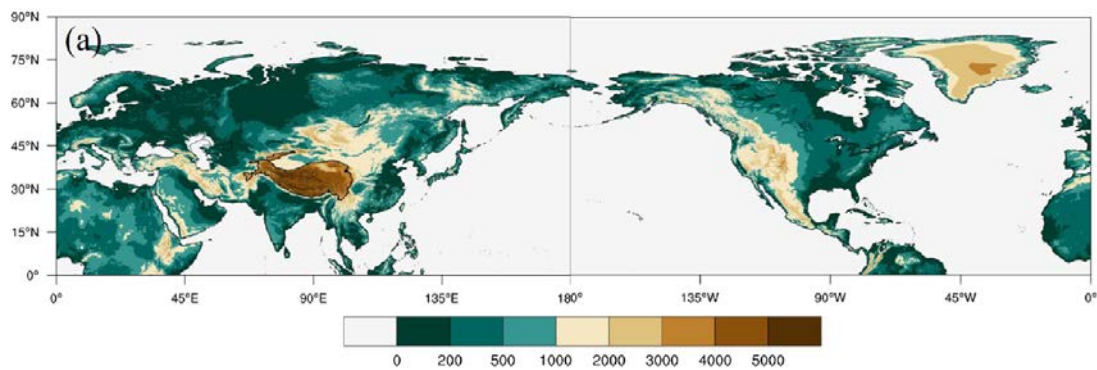
323 HemisphereFigure 7 (d) shows the mean spatial distribution of PBLH – LCL in
 324 the Northern Hemisphere from June to August of 2010-2019. The TP (27-40N,
 325 70-105E) and Rocky Mountains (27-40N, 103-120W) are two typical high value

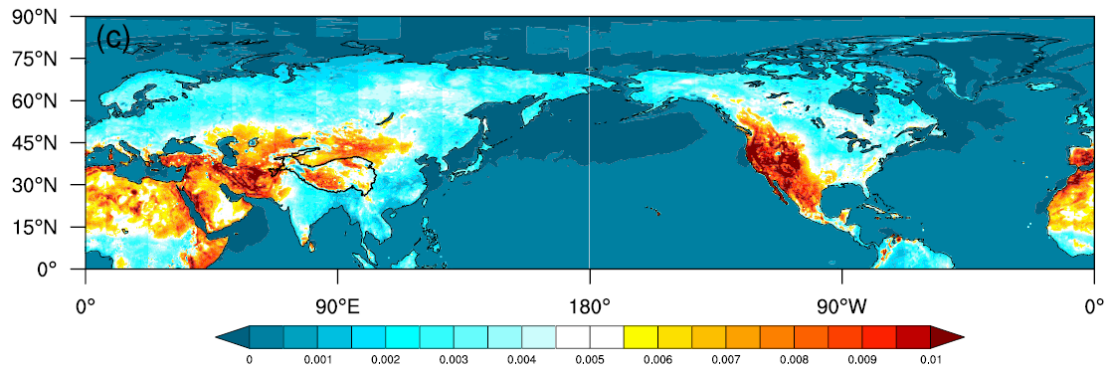
326 regions in the Northern Hemisphere, and the mean PBLH – LCL over the TP and
327 Rocky Mountains are 376.7 m and -101.9 m, respectively.

328 Figure 7 (b)-(c) show the spatial distribution of ST and BT in the Northern
329 Hemisphere from June to August of 2010-2019, respectively. The effect of strong
330 thermal turbulence results in obvious positive value of PBLH – LCL at high elevation
331 regions under low air density condition in the Northern Hemisphere ($BT = 0.008 \text{ m}^2$
332 s^{-3} , $PBLH - LCL = 376.7 \text{ m}$ over the TP and $BT = 0.011 \text{ m}^2 \text{ s}^{-3}$, $PBLH - LCL =$
333 -101.9 m over the Rocky Mountains). Figure 7 (b) also shows that there are strong
334 STs at these two high elevation regions ($ST = 0.087 \text{ m}^2 \text{ s}^{-3}$ over the TP and $ST = 0.085$
335 $\text{m}^2 \text{ s}^{-3}$ over the Rocky Mountains). Both the BT and ST increase significantly at high
336 elevation due to low air density compared to those at low elevation. The above results
337 enlighten us on thinking about whether the triggering effects of large topography and
338 boundary layer turbulence, which reflect the special turbulence characteristics in
339 boundary layer at high elevation regions under low air density condition, can be
340 applicable for any large topography in the globe, including TP and other regions (e.g.
341 Rocky Mountains).

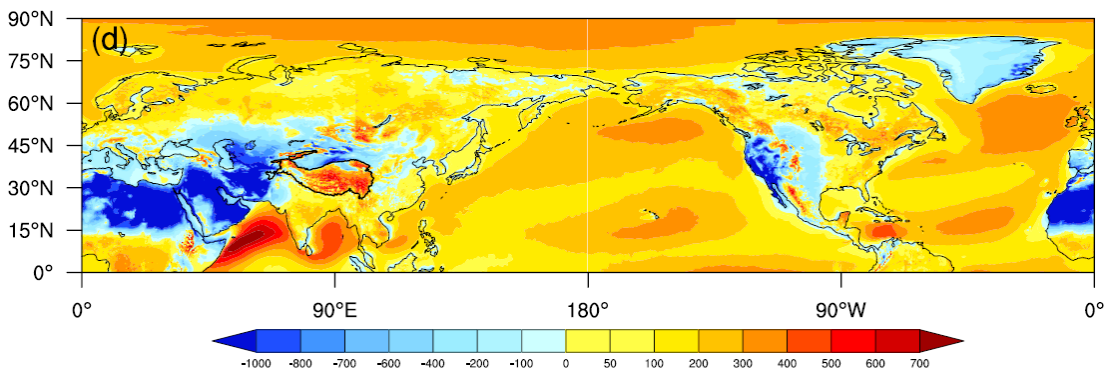
342 Figure 8 shows the conceptual model of atmosphere from the near-surface to
343 upper troposphere over the TP. Compared to the low elevation, the TP is characterized
344 by higher PBLH and lower LCL because of strong BT and ST, which is favorable for
345 the formation of shallow clouds in the afternoon. Meanwhile, the large scale
346 ascending motion over the TP results in the transition from shallow clouds to deep
347 convective clouds in the late afternoon and evening.

348

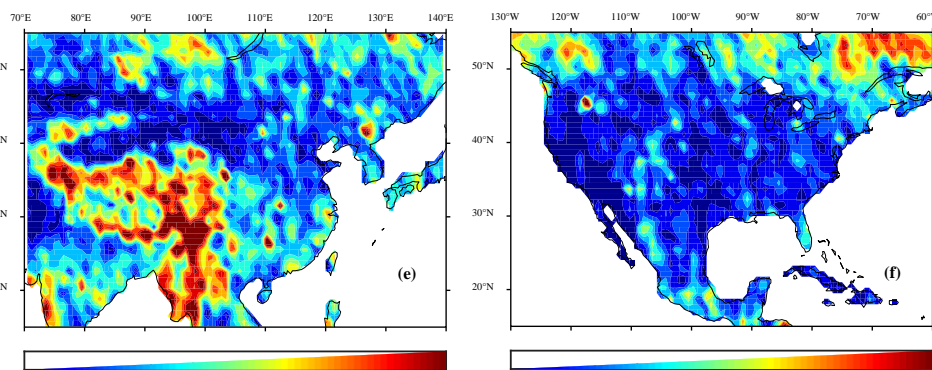




351

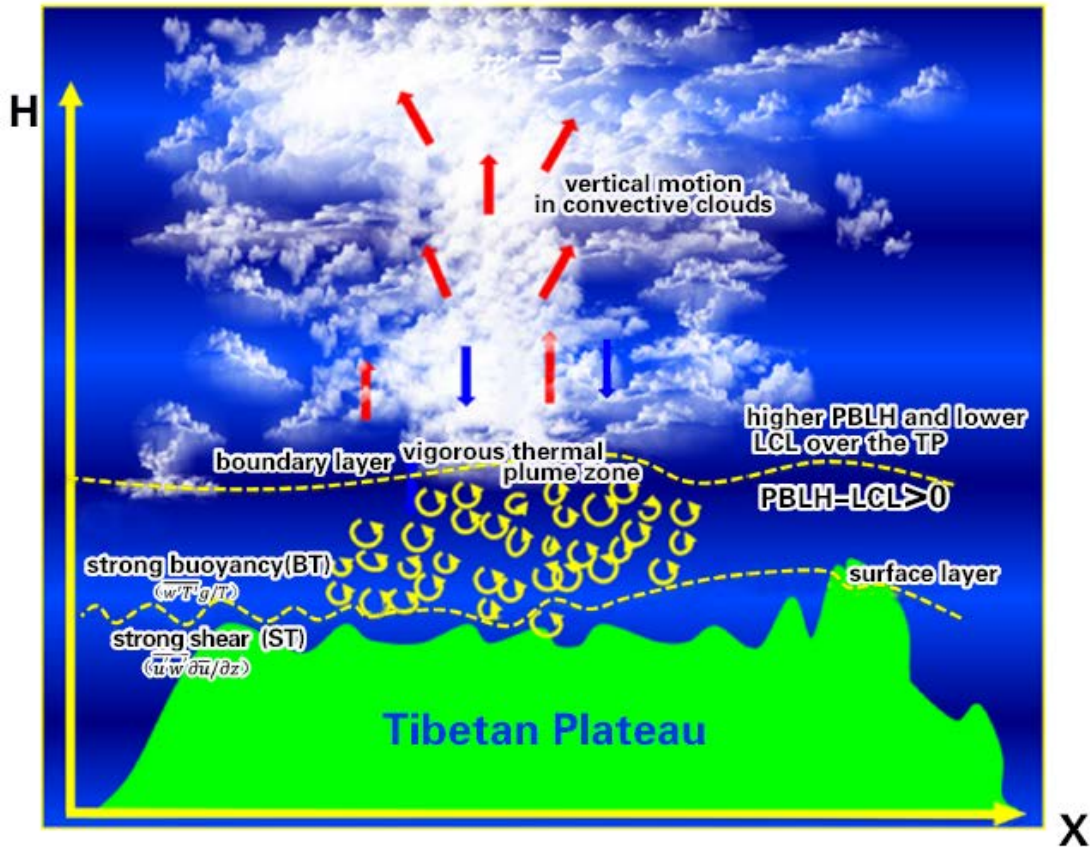


352
353



354

355 Figure 7. The spatial distribution of (a) ground level elevation, (b) ST, (c) BT, and (d)
 356 PBLH-LCL, and (e) LCC derived from ERA5 reanalysis data at local time 2:00 pm in
 357 the Northern Hemisphere in summer. Figure (e) and (f) are the summer mean LCC
 358 derived from cloudsat satellite data at local time 2:00 pm in eastern China and North
 359 America, respectively.



360
 361 Figure 8. The characteristics model of boundary layer turbulence related to “high
 362 efficiency” triggering mechanisms for convection over the TP.

363 **4 Conclusions and further discussion**

364 In this study, we focus on the triggering effects of large topography and
 365 boundary layer turbulence over the Tibetan Plateau on convection. The topography of
 366 TP also has a major role in the increasing of occurrences of convective clouds. Our
 367 results further confirm the conclusions from Wang et al. (2020), which found that
 368 PBLH-LCL over the TP is greater than that in eastern China. Compared to the eastern
 369 China, with the same relative humidity, lower temperature over the TP results in a
 370 lower lifting condensation level. With the same surface sensible heat flux, lower air
 371 density over the TP results in a larger buoyancy flux and a deeper boundary layer. The
 372 observational results show that, under low relative humidity condition ($RH < 40\%$),
 373 the low cloud cover (LCC) is higher than 60% over the TP. In contrast, the high LCC
 374 ($LCC > 60\%$) only appears under conditions with high RH ($RH > 60\%$) at low
 375 elevation.

376 In general, LCC increases with the increasing elevation. The median of LCCs at
 377 high elevation (TP) are significantly greater than those at low elevation (eastern China)
 378 throughout the day. The diurnal variations of LCC in eastern China are generally
 379 distributed in unimodal pattern with the maximum appearing at 2:00 pm BT and low

380 values during the night. The diurnal variations of LCC at high elevation (TP) present
381 a bimodal curve with the maximum appearing at 5:00 pm BT and the secondary local
382 maximum appearing at 8:00 am BT. In addition, LCC maintains at high values at high
383 elevation (TP) during the day. The median cloud top height derived from himawari-8
384 retrieval product shows the transition from shallow clouds to deep convective clouds
385 in the late afternoon and evening over the TP, which is attributed to the strong
386 large-scale ascending motion from the near surface to upper troposphere over the TP.

387 The buoyancy term (BT) and shear term (ST) over the TP are significantly greater
388 than those at the low elevation, which is favorable for the formation of increasing
389 PBLH. Similar phenomenon occurs at other high elevation area (e.g. Rocky
390 Mountains). The strong thermal turbulence results in positive value of PBLH-LCL at
391 high elevation regions under low RH condition in the Northern Hemisphere. The
392 slightly greater than zero PBLH-LCL corresponds spatially to more LCC in the
393 central part of Rocky Mountains, but obvious large-scale subsidence on both sides of
394 the mountain leads to strong inversion above PBL and lower RH in PBL, which
395 further lead to less LCC in these areas. Thus less LCC is generated at Rocky
396 Mountains compared to the TP.

397

398 **Data availability**

399 All reanalysis data used in this study were obtained from publicly available sources:
400 ERA5 reanalysis data can be obtained from the ECMWF public datasets web interface
401 (<http://apps.ecmwf.int/datasets/>). The satellite (CloudSat radar and Calipso
402 lidar)-merged cloud classification product 2B-CLDCLASS-lidar were obtained from
403 Colorado State University
404 (<http://www.cloudsat.cira.colostate.edu/data-products/level-2b/2b-cldclass-lidar>). The
405 himawari-8 retrieval products were obtained from JAXA Himawari Monitor
406 (<https://www.eorc.jaxa.jp/ptree/>).

407 **Code Availability**

408 The data in this study are analysed with MATLAB. Contact Y.W. for specific code
409 requests.

410 **Acknowledgements**

411 Xu and Wang are supported by the Second Tibetan Plateau Scientific Expedition and
412 Research (STEP) program (Grant Nos. 2019QZKK0105), National Natural Science
413 Foundation of China (Grant Nos. 91837310), and the National Natural Science
414 Foundation for Young Scientists of China (Grant Nos. 41805006).

415 **Author Contributions**

416 X.X. and Y. W. led this work with contributions from all authors. Y.T. and Y. W.
417 made the calculations and created the figures. X.X, Y.W. and S.Z. led analyses,
418 interpreted results and wrote the paper.

419 **Competing interests**

420 The authors declare no competing interests.

421

422 **References**

423 Brümmer, B.: Structure, dynamics and energetics of boundary layer rolls from Kon
424 Tur aircraft observations, undefined, 1985.

425 Dyer, A. J.: A review of flux-profile relationships, *Bound.-Layer Meteorol.*, 7, 363–
426 372, <https://doi.org/10.1007/bf00240838>, 1974.

427 Ek, M. and Mahrt, L.: Daytime Evolution of Relative Humidity at the Boundary
428 Layer Top, *Mon. Weather Rev.*, 122, 2709–2721,
429 [https://doi.org/10.1175/1520-0493\(1994\)122<2709:DEORHA>2.0.CO;2](https://doi.org/10.1175/1520-0493(1994)122<2709:DEORHA>2.0.CO;2), 1994.

430 Findell, K. L. and Eltahir, E. A. B.: Atmospheric Controls on Soil Moisture–Boundary
431 Layer Interactions. Part I: Framework Development, *J. Hydrometeorol.*, 4, 552–569,
432 [https://doi.org/10.1175/1525-7541\(2003\)004<0552:ACOSML>2.0.CO;2](https://doi.org/10.1175/1525-7541(2003)004<0552:ACOSML>2.0.CO;2), 2003.

433 Flohn, H. and Reiter, E. R.: Contributions to a meteorology of the Tibetan highlands,
434 1967.

435 Gentine, P., Holtslag, A. A. M., D’Andrea, F., and Ek, M.: Surface and Atmospheric
436 Controls on the Onset of Moist Convection over Land, *J. Hydrometeorol.*, 14, 1443–
437 1462, <https://doi.org/10.1175/JHM-D-12-0137.1>, 2013.

438 Guillod, B. P., Orlowsky, B., Miralles, D. G., Teuling, A. J., and Seneviratne, S. I.:
439 Reconciling spatial and temporal soil moisture effects on afternoon rainfall, *Nat.*
440 *Commun.*, 6, 6443, <https://doi.org/10.1038/ncomms7443>, 2015.

441 Hersbach, H., Bell, B., Berrisford, P., Hirahara, S., Horányi, A., Muñoz-Sabater, J.,
442 Nicolas, J., Peubey, C., Radu, R., Schepers, D., Simmons, A., Soci, C., Abdalla, S.,
443 Abellan, X., Balsamo, G., Bechtold, P., Biavati, G., Bidlot, J., Bonavita, M., Chiara, G.
444 D., Dahlgren, P., Dee, D., Diamantakis, M., Dragani, R., Flemming, J., Forbes, R.,
445 Fuentes, M., Geer, A., Haimberger, L., Healy, S., Hogan, R. J., Hólm, E., Janisková,
446 M., Keeley, S., Laloyaux, P., Lopez, P., Lupu, C., Radnoti, G., Rosnay, P. de, Rozum,
447 I., Vamborg, F., Villaume, S., and Thépaut, J.-N.: The ERA5 global reanalysis, *Q. J. R.*
448 *Meteorol. Soc.*, 146, 1999–2049, <https://doi.org/10.1002/qj.3803>, 2020.

449 Li, Y. and Zhang, M.: Cumulus over the Tibetan Plateau in the Summer Based on
450 CloudSat–CALIPSO Data, *J. Clim.*, 29, 1219–1230,
451 <https://doi.org/10.1175/JCLI-D-15-0492.1>, 2016.

- 452 Luo, Y., Zhang, R., Qian, W., Luo, Z., and Hu, X.: Intercomparison of Deep
453 Convection over the Tibetan Plateau–Asian Monsoon Region and Subtropical North
454 America in Boreal Summer Using CloudSat/CALIPSO Data, *J. Clim.*, 24, 2164–2177,
455 <https://doi.org/10.1175/2010JCLI4032.1>, 2011.
- 456 Romps, D. M. (2017). Exact expression for the lifting condensation level. *Journal of*
457 *the Atmospheric Sciences*, 74, 3891–3900. [https://doi.org/10.1175/JAS-D-17-](https://doi.org/10.1175/JAS-D-17-0102.1)
458 0102.1
- 459 Sassen, K. and Wang, Z.: Classifying clouds around the globe with the CloudSat radar:
460 1-year of results, *Geophys. Res. Lett.*, 35, <https://doi.org/10.1029/2007GL032591>,
461 2008.
- 462 Stull, R. B.: Mean Boundary Layer Characteristics, in: *An Introduction to Boundary*
463 *Layer Meteorology*, edited by: Stull, R. B., Springer Netherlands, Dordrecht, 1–27,
464 https://doi.org/10.1007/978-94-009-3027-8_1, 1988.
- 465 Sugimoto, S. and Ueno, K.: Role of Mesoscale Convective Systems Developed
466 around the Eastern Tibetan Plateau in the Eastward Expansion of an Upper
467 Tropospheric High during the Monsoon Season, *J. Meteorol. Soc. Jpn. Ser II*, 90,
468 297–310, <https://doi.org/10.2151/jmsj.2012-209>, 2012.
- 469 Taylor, C. M., de Jeu, R. A. M., Guichard, F., Harris, P. P., and Dorigo, W. A.:
470 Afternoon rain more likely over drier soils, *Nature*, 489, 423–426,
471 <https://doi.org/10.1038/nature11377>, 2012.
- 472 Tuttle, S. and Salvucci, G.: Empirical evidence of contrasting soil moisture–
473 precipitation feedbacks across the United States, *Science*, 352, 825–828,
474 <https://doi.org/10.1126/science.aaa7185>, 2016.
- 475 Wang, Y., Xu, X., Zhao, T., Sun, J., Yao, W., and Zhou, M.: Structures of convection
476 and turbulent kinetic energy in boundary layer over the southeastern edge of the
477 Tibetan Plateau, *Sci. China Earth Sci.*, 58, 1198–1209,
478 <https://doi.org/10.1007/s11430-015-5054-1>, 2015.
- 479 Wang, Y., Xu, X., Liu, H., Li, Y., Li, Y., Hu, Z., Gao, X., Ma, Y., Sun, J., Lenschow, D.
480 H., Zhong, S., Zhou, M., Bian, X., and Zhao, P.: Analysis of land surface parameters
481 and turbulence characteristics over the Tibetan Plateau and surrounding region, *J.*
482 *Geophys. Res. Atmospheres*, 121, 9540–9560, <https://doi.org/10.1002/2016JD025401>,
483 2016.
- 484 Wang, Y., Zeng, X., Xu, X., Welty, J., Lenschow, D. H., Zhou, M., and Zhao, Y.: Why
485 Are There More Summer Afternoon Low Clouds Over the Tibetan Plateau Compared
486 to Eastern China?, *Geophys. Res. Lett.*, 47, e2020GL089665,
487 <https://doi.org/10.1029/2020GL089665>, 2020.
- 488 Weckwerth, T. M., Wilson, J., Wakimoto, R., and Crook, N. A.: Horizontal convective

489 rolls: Determining the environmental conditions supporting their existence and
490 characteristics, *Mon. Weather Rev.*, 125, 505–526,
491 [https://doi.org/10.1175/1520-0493\(1997\)12560;0505:hcrdte62;2.0.co;2](https://doi.org/10.1175/1520-0493(1997)12560;0505:hcrdte62;2.0.co;2), 1997.

492 Wu, G., Duan, A., Liu, Y., Mao, J., Ren, R., Bao, Q., He, B., Liu, B., and Hu, W.:
493 Tibetan Plateau climate dynamics: recent research progress and outlook, *Natl. Sci.*
494 *Rev.*, 2, 100–116, <https://doi.org/10.1093/nsr/nwu045>, 2015.

495 Xu, X., Zhou, M., Chen, J., Bian, L., Zhang, G., Liu, H., Li, S., Zhang, H., Zhao, Y.,
496 Suolongduoji, and Jizhi, W.: A comprehensive physical pattern of land-air dynamic
497 and thermal structure on the Qinghai-Xizang Plateau, *Sci. China Ser. D*, 45, 577–594,
498 <https://doi.org/10.1360/02yd9060>, 2002.

499 Xu, X., Zhang, R., Koike, T., Lu, C., Shi, X., Zhang, S., Bian, L., Cheng, X., Li, P.,
500 and Ding, G.: A New Integrated Observational System Over the Tibetan Plateau, *Bull.*
501 *Am. Meteorol. Soc. - BULL AMER METEOROL SOC*, 89, 1492–1496,
502 <https://doi.org/10.1175/2008BAMS2557.1>, 2008.

503 Xu, X., Shi, X., and Lu, C.: Theory and application for warning and prediction of
504 disastrous weather downstream from the Tibetan Plateau, *Theory Appl. Warn. Predict.*
505 *Disastrous Weather Downstr. Tibet. Plateau*, 1–116, 2012.

506 Xu, X., Zhao, T., Lu, C., Guo, Y., Chen, B., Liu, R., Li, Y., and Shi, X.: An important
507 mechanism sustaining the atmospheric “water tower” over the Tibetan Plateau,
508 *Atmospheric Chem. Phys.*, 14, 11287–11295,
509 <https://doi.org/10.5194/acp-14-11287-2014>, 2014.

510 Yi, C., and Guo, X.: Characteristics of convective cloud and precipitation during
511 summer time at Naqu over Tibetan Plateau (in Chinese), *Chinese Science Bulletin*, 61,
512 1706–1711, <https://doi.org/10.1360/N972015-01292>, 2016.

513 Young, G. S.: Convection in the atmospheric boundary layer, *Earth-Sci. Rev.*, 25,
514 179–198, [https://doi.org/10.1016/0012-8252\(88\)90020-7](https://doi.org/10.1016/0012-8252(88)90020-7), 1988a.

515 Young, G. S.: Turbulence Structure of the Convective Boundary Layer. Part I.
516 Variability of Normalized Turbulence Statistics, *J. Atmospheric Sci.*, 45, 719–726,
517 [https://doi.org/10.1175/1520-0469\(1988\)045<0719:TSOTCB>2.0.CO;2](https://doi.org/10.1175/1520-0469(1988)045<0719:TSOTCB>2.0.CO;2), 1988b.

518 Zhou, M., Xu, X., Bian, L., Chen, J., Liu H., Zhang, H., Li, S., and Zhao J.:
519 Observational analysis and dynamic study of atmospheric boundary layer on Tibetan
520 Plateau (in Chinese), 125 pp., 2000.

521